

A Comparison of K_u -Band Doppler Measurements at 20° Incidence With Predictions From a Time-Dependent Scattering Model

D. R. THOMPSON AND B. L. GOTWOLS

Applied Physics Laboratory, Johns Hopkins University, Laurel, Maryland

W. C. KELLER

U.S. Naval Research Laboratory, Washington, D. C.

The analysis of coherent K_u -band radar data measured from the Chesapeake Bay Light Tower as part of the SAXON Experiment in September–October 1988 is discussed. We concentrate on a 20-min data segment collected at an incidence angle of 20° for both V - V and H - H polarization. Average Doppler spectra are estimated for each second of the data. These Doppler spectra show a large variation in center frequency and relative power due to the influence of the longwave surface on the backscattered field. The basic assumptions and approximations used in the formulation of a time-dependent scattering model are briefly presented, and concurrent measurements of the longwave surface spectrum at the tower are input into this model in order to calculate the expected mean Doppler spectra. These calculated spectra show very good agreement with the measurements. Implications of the measurements and calculations concerning future experiments and refinements to the model are also discussed.

1. INTRODUCTION

In recent years, much attention has been given to understanding how microwave radar is scattered from the ocean surface [see *Plant and Keller, 1990* and references therein]. In particular, it has been found that by examining the coherence properties of the backscattered field, usually in the form of Doppler spectra, a great deal can be inferred about the properties of the ocean surface. Most of the Doppler data collected to date are at incidence angles greater than about 45° .

In a recent paper [*Thompson, 1989*] we developed a time-dependent scattering model and discussed the dependence of computed Doppler spectra on such parameters as wind velocity, incidence and aspect angle, and frequency. This model reduces to the proper specular and small-perturbation limits for V - V and H - H polarization, and its time dependence is based on the assumption of linear surface evolution. The width of the computed spectra increases with increasing radar frequency and decreasing incidence angle due primarily to the motion of the longwave surface. This motion also produces a shift in the spectral peak away from the Bragg frequency. This shift, which is largest at lower incidence angles and higher radar frequencies, is also due to the effect of longwave motion on the backscattered field. At incidence angles $\geq 45^\circ$, the calculations are in good general agreement with the data.

We discuss in this paper the properties of K_u -band Doppler spectra measured from the Chesapeake Bay Light Tower during the SAXON Experiment in September–October 1988. These data, taken at an incidence angle of 20° at both V - V and H - H polarization, represent a large fraction of the low-incidence angle K_u -band Doppler measurements available at this time. A comparison of our model predictions

with this recent K_u -band data provides a stringent test of our understanding of the physics of microwave scattering from the ocean surface. In the following section we describe the experimental setup during the SAXON Experiment and also discuss the radar data acquisition and digitization. In section 3 we describe our scattering model, and in section 4 we compare the measured data with model predictions. Finally, in section 5 we present a summary of our findings and suggestions for further measurements and analysis.

2. EXPERIMENTAL SETUP AND DATA ACQUISITION

The 1988 SAXON Experiment is part of an ongoing research program sponsored by the U.S. Office of Naval Research (ONR) to understand the physics of microwave scattering from the ocean surface. A detailed description of the various measurement activity during the SAXON Experiment may be found in the work by *Shemdin [1989]*. In the present paper we will focus our description on the K_u -band radar and the other sensors relevant to the measurements required in our analysis.

A schematic of the experimental radar setup at the Chesapeake Bay Light Tower is shown in Figure 1. The incident beam was generated by a dual-polarized K_u -band (14.0 GHz) CW radar attached to a railing on the helicopter deck of the tower ≈ 27 m above the mean water level. The radar makes an incidence angle of 20° with the vertical, and produces a spot on the surface roughly 1.5 m on a side. For each polarization, the receiver consisted of two channels that provided in-phase and quadrature-phase (I and Q) baseband signals. When processed properly, these signals allow the unfolded Doppler spectrum for both positive and negative frequencies to be recovered without the need for a frequency offset.

In the present paper we will concentrate our analysis on the data collected between about 0820 and 0845 eastern daylight time (EDT) on 11 October, 1988. As can be seen from Figure 1, the radar was looking toward 260° T (260°

Copyright 1991 by the American Geophysical Union.

Paper number 90JC02210.
0148-0227/91/90JC-02210\$05.00

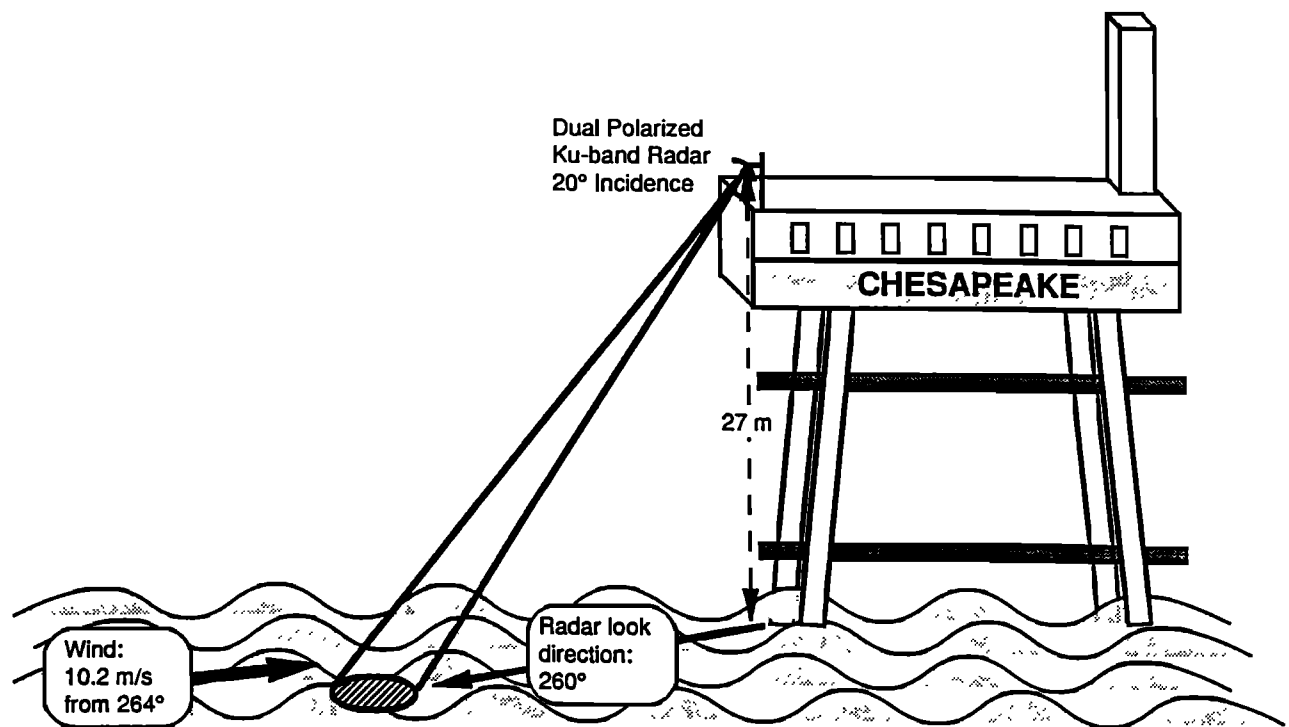


Fig. 1. Schematic of the radar setup.

with respect to true North), and the wind was blowing at 10.2 m/s from 264° T during this time period. Thus the radar was looking almost directly into the wind. The wind measurements were made from an anemometer located at the top of the tower about 42 m above the ocean surface. Radar data for other wind conditions were also collected and will be reported in a future paper.

Various sensors for directly measuring the surface wave frequency spectrum were also deployed during SAXON. In particular, a bottom-mounted pressure sensor array [Herbers and Guza, 1990] and a wire wave gauge [Melville et al., 1989] provided local measurements of the structure of the longwave surface including directional resolution of the wind-wave and swell components. As we will see later, these measurements are critical inputs to our scattering model.

Current measurements from an electromagnetic-type current meter mounted at a depth of 5 m below the surface were also part of the environmental characterization made during SAXON [Abreu et al., 1990]. We have used these measurements of both components of the horizontal current to compute the average water velocity during the ≈ 20 -min duration of the radar collection of interest. This velocity was 0.14 m/s toward East, and 0.07 m/s toward North. In addition, there was a mean surface drift that we have estimated to be $\approx 3\%$ of the wind speed; i.e., ≈ 0.3 m/s toward the radar. (We will see later that these mean surface currents agree with those measured directly by the radar.) We summarize in Table 1 some of the pertinent facts concerning the experimental setup discussed above.

We turn now to a brief discussion of the data acquisition. The in-phase (I) and quadrature (Q) signals from the radar were recorded on a Hewlett Packard FM tape recorder running at a speed of $1\frac{1}{8}$ in/s (4.8 cm/s). No attempt was made at an absolute calibration of the system. Thus the I and Q signals are proportional to the backscattered field to within

an unknown multiplicative constant (which was different for the I and Q channels). The tape recorder was calibrated by sequentially injecting two known DC voltages and a 500-Hz sine wave. All measurements to be reported in this paper are referred to the input of the tape recorder. In other words, the tape recorder calibrations have been applied to the digitized data.

Digitizing the analog tape was accomplished using a Metrabyte Dash-16 A/D card with 12-bit resolution installed in a COMPAQ Desk Pro 286 computer. In order to minimize timing skew between the digitized I and Q channels, which theoretically should be sampled simultaneously, a special clocking scheme was devised that sampled a sequence of channels every 25 μ s and then paused until the next channel scan was required. Eight files were stored on several 20-Mbyte Bernoulli disks and subsequently transferred to a VAX 11/750 computer for analysis.

TABLE 1. Pertinent Facts

Parameter	Value
Radar frequency	14 GHz ($\lambda = 0.02$ m)
Radar footprint	$\approx 1.5 \times 1.5$ m
Incidence angle	20°
Look direction	toward 260° T
Radar Bragg frequency	8.1 Hz
Doppler velocity conversion	32 Hz/(m/s)
Wind speed	10.2 m/s
Wind direction	from 264° T
Swell direction	toward 270° T
Mean water depth	12.2 m
Mean surface velocity	
North component	0.07 m/s
East component	0.14 m/s
Estimated wind drift	0.3 m/s toward radar

3. TIME-DEPENDENT SCATTERING MODEL

A primary goal of this work was to compare the measured Doppler spectra with predictions from our time-dependent scattering model. This model has been discussed by *Thompson* [1989], so here we will simply review briefly its main features. We have started from an expression for the scattered field derived from two iterations of the surface-current integral equation retaining all terms up to first order in the surface slope [*Holliday*, 1987]. This expression is simplified considerably by assuming that the surface height $\eta(\mathbf{x}, t)$ at position $\mathbf{x}(=x, y)$ on the horizontal plane) and time t may be separated into long scales specified by $\eta_L(\mathbf{x}, t)$ and short scales specified by $\eta_S(\mathbf{x}, t)$ such that

$$\eta(\mathbf{x}, t) = \eta_L(\mathbf{x}, t) + \eta_S(\mathbf{x}, t) \quad (1)$$

with

$$2\kappa_z \eta_S(\mathbf{x}, t) \ll 1 \quad (2)$$

Using this definition for the long and short scales, we obtain the equation

$$\begin{aligned} \mathbf{B}(\mathbf{r}_0, t) = & \frac{1}{2\pi i} \frac{e^{i\kappa r_0}}{r_0} \int G(\mathbf{x}) \exp[-2i\kappa_H \cdot \mathbf{x} \\ & - 2i\kappa_z \eta_L(\mathbf{x}, t)] \times \left\{ [\kappa_z - \kappa_H \cdot \nabla \eta_L(\mathbf{x}, t)] \right. \\ & \cdot [1 - 2i\kappa_z \eta_S(\mathbf{x}, t)] \mathbf{B}_0 + 2\mathbf{B}_0 \\ & \left. \cdot [\hat{\mathbf{e}}_z \times \nabla \eta_S(\mathbf{x}, t)] \frac{\kappa_H \times \kappa}{\kappa_z} \right\} d\mathbf{x} \quad (3) \end{aligned}$$

for the backscattered magnetic field. (For all computations to be presented in this paper, we assume that the ocean is a perfect conductor.) In this equation, κ_H and κ_z are the horizontal and vertical components of the radar wave vector κ , respectively, \mathbf{B}_0 specifies the incident field strength and polarization, $G(\mathbf{x})$ describes the antenna footprint, $\hat{\mathbf{e}}_z$ is a unit vector along the (vertical) z axis, and r_0 is the distance from the center of the footprint to the antenna. As discussed by *Thompson* [1989], (3) yields the proper expression for the scattered fields in both the long-scale ($\eta_S(\mathbf{x}, t) = 0$) and short-scale ($\eta_L(\mathbf{x}, t) = 0$) limits [*Valenzuela*, 1978].

For a deterministic surface, one may compute the backscattered field directly from (3). For most cases, however, the surface cannot be specified completely and one must resort to a statistical description. In this case one may assume, for example, that $\eta_L(\mathbf{x}, t)$ and $\eta_S(\mathbf{x}, t)$ are zero-mean Gaussian random processes and that $\langle \eta_L(\mathbf{x}, t) \eta_S(\mathbf{x}, t) \rangle = 0$. These assumptions do not necessarily mean that the scattered field, $\mathbf{B}(\mathbf{r}, t)$, is also Gaussian since $\eta_L(\mathbf{x}, t)$ appears nonlinearly in (3). If we are dealing with a surface for which $\eta_L(\mathbf{x}, t) = 0$ (that is a surface with small-scale roughness only) then \mathbf{B} is linear in $\eta_S(\mathbf{x}, t)$ and hence also Gaussian. Even when $\eta_L(\mathbf{x}, t)$ is not small, the illuminated area on the surface may contain enough independent scattering centers so that the received field is still nearly Gaussian due to the central-limit theorem. In general, we expect the backscattered field to become more non-Gaussian as the mean-squared surface height increases and as the antenna footprint decreases. An examination of the statistics of our SAXON

data has provided insight into some of these questions. We will report our findings on this topic in a future publication.

With the above assumptions about the behavior of $\eta(\mathbf{x}, t)$, we may now write the autocovariance, $R(t)$, of the backscattered field as

$$R(t) = \frac{4\pi r_0^2}{|\mathbf{B}_0|^2 A_{\text{eff}}} \langle \mathbf{B}^*(r_0, 0) \cdot \mathbf{B}(r_0, t) \rangle \quad (4)$$

where A_{eff} is the effective area of the footprint, and we have normalized $R(t)$ so that $R(0)$ is the mean cross section per unit area. Using (3) and the assumed independence of $\eta_L(\mathbf{x}, t)$ and $\eta_S(\mathbf{x}, t)$, we find that $\langle \mathbf{B}^* \cdot \mathbf{B} \rangle$ may be written in the form of a Fourier transform of the product of a function which depends on $\eta_L(\mathbf{x}, t)$ times a function which depend on $\eta_S(\mathbf{x}, t)$. The convolution theorem may therefore be used to write (4) in the form

$$R(t) = R_{SP}(t) + R_{TB}(t) \quad (5)$$

where

$$R_{SP}(t) = \frac{1}{\pi} \mathcal{G}_2(2\kappa_H, \kappa_z, t) \quad (6)$$

and

$$\begin{aligned} R_{TB}(t) = & \frac{2}{\pi} \int \{ \kappa_z^2 \mathcal{G}_2(\mathbf{k} - 2\kappa_H, \kappa_z, t) \\ & + \kappa_H^2 [\hat{\mathbf{B}}_0 \cdot (\hat{\mathbf{e}}_z \times \mathbf{k})]^2 \mathcal{G}_0(\mathbf{k} - 2\kappa_H, \kappa_z, t) \} \\ & \times [\psi_S(\mathbf{k}) e^{-i\omega t} + \psi_S(-\mathbf{k}) e^{i\omega t}] d\mathbf{k} \quad (7) \end{aligned}$$

and we have assumed that κ lies in the x - z plane. Also in (7), $\hat{\mathbf{B}}_0$ is a unit vector in the direction of \mathbf{B}_0 . (We use the subscripts *SP* and *TB* in (5)–(7) to emphasize the correspondence of these expressions with the familiar “specular” and “tilted Bragg” terms [*Valenzuela*, 1978].) The shortwave spectral density, $\psi_S(\mathbf{k})$, which appears in (7), is related to the autocovariance of the shortwave portion of the surface through

$$\langle \eta_S(0, 0) \eta_S(\mathbf{x}, t) \rangle = \int \psi_S(\mathbf{k}) \cos(\mathbf{k} \cdot \mathbf{x} - \omega t) d\mathbf{k} \quad (8)$$

A similar expression

$$\langle \eta_L(0, 0) \eta_L(\mathbf{x}, t) \rangle = \int \psi_L(\mathbf{k}) \cos(\mathbf{k} \cdot \mathbf{x} - \omega t) d\mathbf{k} \quad (9)$$

applies for the longwave surface. Note that these expressions along with (1) and our assumption that $\eta_L(\mathbf{x}, t)$ and $\eta_S(\mathbf{x}, t)$ are statistically independent imply that the total wave-height spectrum, $\psi(\mathbf{k})$, is given by

$$\psi(\mathbf{k}) = \psi_L(\mathbf{k}) + \psi_S(\mathbf{k}) \quad (10)$$

The influence of the longwave portion of the surface on the scattering is contained in the functions \mathcal{G}_0 and \mathcal{G}_2 in (6)–(7). These functions are derived from a stationary phase approximation similar to that discussed by *Thompson* [1988]. They are related to the various second moments of $\psi_L(\mathbf{x}, t)$ and are given explicitly by

$$\mathcal{G}_0(\mathbf{k}, \kappa_z, t) = \int H(\mathbf{x}) \exp(-i\mathbf{k} \cdot \mathbf{x}) \times \exp\{-2\kappa_z^2[\overline{S_x^2}x^2 + \overline{S_y^2}y^2 + \overline{V^2}t^2 + 2\overline{S_{xy}}xy - 2(\alpha x + \beta y)t]\} d\mathbf{x} \quad (11)$$

$$\mathcal{G}_2(\mathbf{k}, \kappa_z, t) = \left[\kappa_z^2 + \kappa_H \cdot \mathbf{k} + \frac{(\kappa_H \cdot \mathbf{k})^2}{4\kappa_z^2} \right] \mathcal{G}_0(\mathbf{k}, \kappa_z, t) \quad (12)$$

The function $H(\mathbf{x})$ in (12) is related to the footprint area and the moments of ψ_L in the exponential term in \mathcal{G}_0 are given by

$$\overline{S_x^2} = \int \psi_L(\mathbf{k})k_x^2 d\mathbf{k} \quad (13a)$$

$$\overline{S_y^2} = \int \psi_L(\mathbf{k})k_y^2 d\mathbf{k} \quad (13b)$$

$$\overline{S_{xy}} = \int \psi_L(\mathbf{k})k_xk_y d\mathbf{k} \quad (13c)$$

$$\overline{V^2} = \int \psi_L(\mathbf{k})\omega^2 d\mathbf{k} \quad (13d)$$

$$\alpha = \int \psi_L(\mathbf{k})k_x\omega d\mathbf{k} \quad (13e)$$

$$\beta = \int \psi_L(\mathbf{k})k_y\omega d\mathbf{k} \quad (13f)$$

The above equations specify the scattering process in terms of the longwave and shortwave portions of the surface wave spectral density. The time dependence in these equations is based on the assumption that each component of the ocean surface wave spectrum evolves in time according to the free wave dispersion relation. This assumption, which is in turn related to the assumption of Gaussian surface displacements, implies that $\omega(\mathbf{k})$ in (8)–(9) is given by

$$\omega(\mathbf{k}) = \left[gk \left[1 + \left(\frac{k}{k_0} \right)^2 \right] \tanh(kD) \right]^{1/2} + \mathbf{k} \cdot \mathbf{U} \quad (14)$$

where g is the acceleration of gravity, $k_0 = 363$ rad/m, D is the water depth, and \mathbf{U} is any background current which may be present. No interaction of the short surface waves with the longwave orbital velocity has been included in our model. However, the short waves do feel the heaving motion of the longwave surface. Comparisons of our model predictions with the SAXON data will give us some indication of how correct our approximations are, at least for K_u -band at 20° incidence.

Finally, we should discuss the separation wave number that divides the spectrum into shortwave and longwave regions. Since the inequality which defines short waves in (2) depends on the z component of the radar wave number, the separation wave number will be frequency dependent. It was found by Thompson [1988] that this separation wave number should be chosen to be $\approx \frac{1}{3}$ the Bragg wave number. We therefore choose this same separation wave number for all the computations to be presented in the present work. With this definition the moments defined by (13a)–(13f) will, in general, also be functions of the radar frequency.

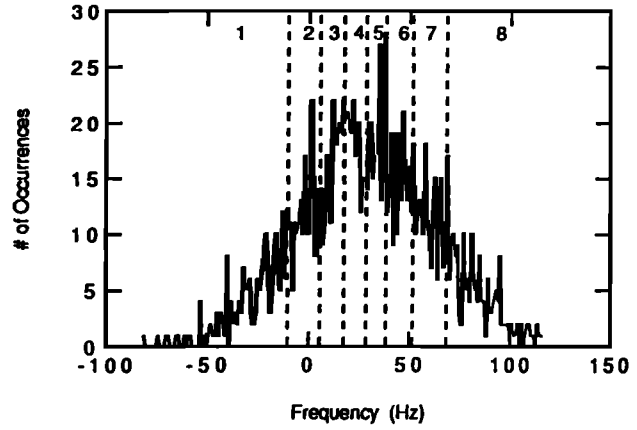


Fig. 2. Histogram of 1-s average vertical polarization Doppler frequency. The dashed lines divide the data into eight equally populated frequency bins.

4. DATA ANALYSIS AND MODEL COMPARISON

In this section we discuss our analysis of the SAXON radar data, and in particular, we show comparisons of the “measured” and predicted Doppler spectra. The Doppler spectrum, $S(\omega)$, is simply the Fourier transform of the autocovariance function $R(t)$. This function is obtained directly from the measured data using (4) and is predicted from (5)–(7). $S(\omega)$ is given explicitly by

$$S(\omega) = \int_{-\infty}^{\infty} e^{-i\omega t} R(t) dt \quad (15)$$

It was necessary to calibrate the raw I and Q data before computing Doppler spectra because the gain in the tape recorder varied from one channel to the next. This calibration prevented the so-called image spectrum corruption of our measured spectra. After performing this calibration, we computed a sample Doppler spectrum for each second of data (1000 I and Q samples sampled at 1 kHz) during the entire run for both $V-V$ and $H-H$ polarization. (Since the autocovariance function $R(t)$ falls to zero in about 20 or 30 ms, the 1-s data samples which were used to generate the histogram in Figure 2 are more than long enough for a meaningful Doppler estimate.) A running 1-s average frequency was also computed for the radar time series essentially by counting rotations of the phase of the I and Q signal. It is important to understand the difference between the 1-s Doppler spectra and the running average frequency time series. The latter was computed from phase information only (counting phase rotations) and thus does not depend on any amplitude changes in the raw I and Q data. The 1-s Doppler spectra, on the other hand, were obtained from a Fourier transform of sequential 1-s-long segments of the I and Q time series, and thus are functions of both amplitude and phase. The running 1-s Doppler spectra and average frequency time series are the basic data products with which we will be concerned in the remainder of our discussion.

We show in Figure 2 a histogram of the number of occurrence of each frequency in the vertical polarization frequency time series mentioned above. Results for the horizontal polarization channel are virtually identical. One can see from this figure that a significant fraction of the data

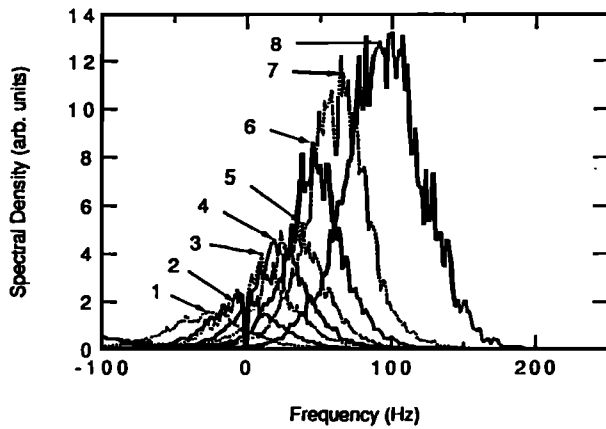


Fig. 3. Average vertical polarization Doppler spectra at various locations along the longwave phase.

has frequencies that are quite different from the ≈ 28 -Hz center frequency. This is, of course, because the motion of the longwave surface is playing an important role in the scattering, and the frequency at any particular time depends on what portion of the longwave phase happens to be passing through the radar footprint at that time. We have partitioned the range spanned by the Doppler frequencies in Figure 2 into eight bins, each of which contains an equal number of samples. The vertical dashed lines in Figure 2 show the boundaries of these frequency bins. One can interpret the field samples in these bins as having been scattered from the phase position on the long wave whose Doppler frequency is equal to the average value for that bin. The highest frequency bin, bin 8, for example, contains samples of the field scattered from the phase position which has the largest velocity component toward the radar. The mean frequency and full width at half maximum of the data in Figure 2 are 28 Hz and 77 Hz, respectively. Thus the histogram provides a useful measure of the frequency shifts induced in the backscattered radar return by the motion of the surface independent of any changes in power which may occur (due to tilt modulation, for example) across the phase of the long wave. Finally, one should note that the mean frequency of the data in Figure 2 is not zero as one would expect if the frequency shift were due only to longwave orbital motion. The observed 28 Hz offset is due to the fact that there was also a mean surface drift toward the radar during the experiment (corresponding to the $\mathbf{k} \cdot \mathbf{U}$ term in (14)) which, along with the motion of the Bragg scatterers, was responsible for the mean Doppler offset seen in Figure 2. This offset, measured directly by the radar, is in good agreement with our estimates based on the current meter measurements and mean Bragg-wave motion discussed earlier (see Table 1), and also gives us confidence that any systematic errors in computing the running 1-s Doppler frequency were quite small.

Using fast Fourier transform techniques, we have computed an average Doppler spectrum for each of the frequency bins in the histogram of Figure 2 by averaging all the 1-s Doppler spectra corresponding to that particular bin. The eight spectra constructed in this way are shown in Figure 3. They are labeled by their corresponding bin number from Figure 2, and the arrows locate the approximate peak position of each spectrum. Notice that the area under these conditionally sampled Doppler spectra increase as the center

frequency increases. The spectrum with the highest Doppler shift, ≈ 90 Hz, comes from the vicinity of the front face of the long wave where the effective incidence angle is smallest and the surface has its maximum (positive) velocity component along the radar line of sight. The spectrum in Figure 3 with the lowest center frequency, ≈ -30 Hz, has the smallest power and results from scattering from the conjugate phase position on the back face of the wave where the line-of-sight velocity takes on its maximum negative value. This change in backscattered power across the phase of the long wave can be characterized by a modulation transfer function (see, for example, *Alpers et al.* [1981] or *Plant* [1989]) which, in general, contains the effect of hydrodynamic modulation of the short-scale Bragg waves by the longwave orbital currents as well as the effect of the changing slope (tilt modulation) discussed above. At 20° incidence, we expect that tilt modulation should be dominant. Note also in Figure 3 that the center frequencies of the largest and smallest spectra are not symmetric about zero frequency. This asymmetry is caused by the mean surface flow and Bragg wave motion as discussed above.

We have normalized the eight spectra in Figure 3 to unit area, and have found that the full widths at half the maximum of each of the spectra are fairly constant with a mean value of about 50 Hz; the central bins are somewhat narrower and the extreme high- and low-frequency bins are somewhat broader. This small variation could be a reflection of the hydrodynamic modulation discussed above, but we feel that it is most probably due to the fact that the extreme bins covered a greater range of average frequencies. The half widths of these spectra are determined by the mean-squared velocity (along the radar line of sight) of the surface waves shorter than the radar footprint. Since this velocity is proportional to the integral of ω^2 times the height spectrum of these subresolution surface waves, our data seem to suggest that this portion of the spectrum does not change very much over the phase of the longwave field. Any change in the subresolution spectrum over the longwave phase would show up as a change in the width of these conditionally sampled Doppler spectra. (Note that there are, in general, two phase locations on the long wave that correspond to a given slope and line-of-sight velocity.) It will be interesting to examine more such Doppler spectra collected at different incidence angles, wind conditions, footprint sizes, and radar frequencies to see how this result depends on such parameters. The character of these conditionally sampled Doppler spectra plays an important role in synthetic aperture radar imaging of the moving ocean surface [*Alpers et al.*, 1981]. As a cross check of our analysis, we have computed the average of these normalized spectra. As expected, the mean frequency and width of this average closely resembles that of the frequency histogram in Figure 2.

In Figure 4 we show the average Doppler spectrum for both *V-V* and *H-H* polarization. These spectra were obtained by averaging the 1-s *V-V* and *H-H* spectra discussed above. We will call these spectra the mean Doppler spectra (as opposed to the 1-s averaged spectra). At the right edge of Figure 4, we show error bars representing the 95% confidence interval for typical high, mid range, and low data values. These error estimates are based on the assumption of a χ^2 distribution with $2N$ degrees of freedom where N ($=1556$) is the total number of 1-s Doppler spectra which have been averaged to produce this figure. The frequency

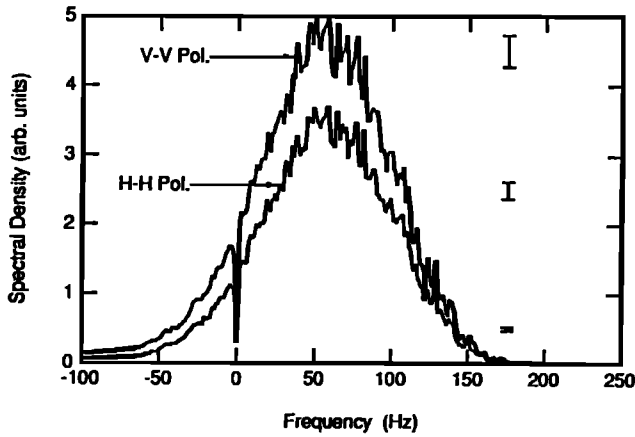


Fig. 4. Mean Doppler spectra for vertical and horizontal polarization.

resolution of the spectra is 1 Hz. Since our radar was not absolutely calibrated, the ordinate units in Figure 4 are arbitrary. In general, the ratio of area under the $H-H$ and $V-V$ Doppler spectra reflect the corresponding power ratio, σ_{HH}/σ_{VV} . For the data in Figure 4, this ratio is about 0.72. In the limiting case where only Bragg waves contribute to the scattering, σ_{HH}/σ_{VV} would be 0.63 at 20° incidence. For purely specular scattering, the ratio would be unity. Since the relative calibration between the $V-V$ and $H-H$ channels (and therefore the polarization ratio) for our radar is accurate to about ± 2 dB, the measured polarization ratio tells us very little about the scattering mechanism.

One can see from Figure 4 that the center frequencies of the mean spectra are about 58 Hz, and the full width at half maximum is about 98 Hz for both polarizations. (The DC notch seen in the measured spectra shown in Figure 4 is an instrumental artifact and has nothing to do with the measured backscatter from the ocean surface.) The center frequency and width of these mean spectra are determined by the average of the 1-s spectra. This average is dominated by the high cross section spectra on the front face of the wave where the line-of-sight velocity is highest, causing the center frequency of the mean spectra to be considerably higher than the 28-Hz centroid of the histogram in Figure 2. The width of the mean spectra is likewise determined by the frequency excursions of the 1-s spectra, again weighted by the relative power associated with each. Note that both the $V-V$ and $H-H$ spectra exhibit a small but noticeable negative-frequency tail, the cause of which we presently do not understand.

We now want to see if our scattering model discussed in section 3 can explain the characteristics of the measured mean Doppler spectra. To accomplish this, we need to specify the form of the surface wave power spectrum $\psi(\mathbf{k})$ to use in our model. In most cases this is not possible because two-dimensional (2D) measurements of $\psi(\mathbf{k})$ over the full range of spatial scales present in the ocean surface are so difficult. What one usually does is resort to an empirical description of $\psi(\mathbf{k})$ in terms of the wind or friction velocity. During SAXON, however, measurements of the longwave frequency spectrum were in fact available from a pressure sensor array [Herbers and Guza, 1990] as well as from wire wave gauge measurements [Melville et al., 1989]. Furthermore, the pressure sensor array also provided estimates of the angular dependence of the long waves and enabled us to

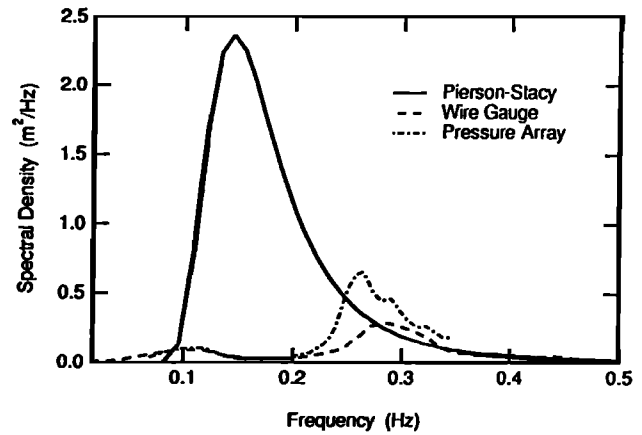


Fig. 5. Comparison of the Pierson-Stacy surface wave frequency spectrum for a wind speed of 10.2 m/s with direct spectral measurements at the SAXON tower.

distinguish swell from wind waves. We will show in what follows that our predicted Doppler spectra are quite sensitive to the power contained in the longwave portion of the surface wave spectrum.

Figure 5 shows a comparison of the empirical Pierson-Stacy frequency spectrum [Pierson and Stacy, 1973] as modified by Bjerkaas and Riedel [Bjerkaas and Riedel, 1979] corresponding to the measured wind speed of 10.2 m/s with actual wave-height spectra measured at the SAXON tower. The dotted curve shows the frequency spectrum measured with the wire wave gauge [Melville et al., 1989], while the dashed curve shows the measured spectrum from the pressure sensor array [Herbers and Guza, 1990]. The pressure sensor data were collected concurrently with the radar data, while the wave gauge data were collected at 1031 EDT, nearly 2 hours after the radar measurements. One can see from Figure 5 that in the lower frequency region (≈ 0.1 to 0.2 Hz), both of the measured spectra are almost an order of magnitude smaller than the empirical spectrum. The peak in the wire gauge spectrum at ≈ 0.27 Hz is about a factor of 2 or so lower than that from the pressure array. We attribute this difference to the fact that the wind speed was dropping during the data collection period, and the wire gauge data were collected at a later time. (In fact, the pressure sensor data collected at 1016 EDT are in good agreement with the wire gauge data collected at 1031 EDT.) At higher frequencies the measured spectra seem to merge rather well with the empirical spectrum which in this region begins to decrease like ω^{-5} .

In the calculations to be presented below, we have assumed that the 2D wave number spectrum of the surface has the form

$$\psi(\mathbf{k}) = \chi(|\mathbf{k}|)\mathcal{F}(\phi_k) \quad (16)$$

where ϕ_k is the direction of \mathbf{k} . For the function $\chi(|\mathbf{k}|)$ in (16) we may then choose either the empirical Pierson-Stacy form over the entire wave number range or convert the measured frequency spectra to wave number spectra and substitute these "measured" data for the Pierson-Stacy values in the appropriate wave number region. (In what follows, we will refer to spectra constructed in this manner from the measured data as augmented spectra.) We choose the angular dependence of the wind waves, $\mathcal{F}(\phi_k)$, to have the form

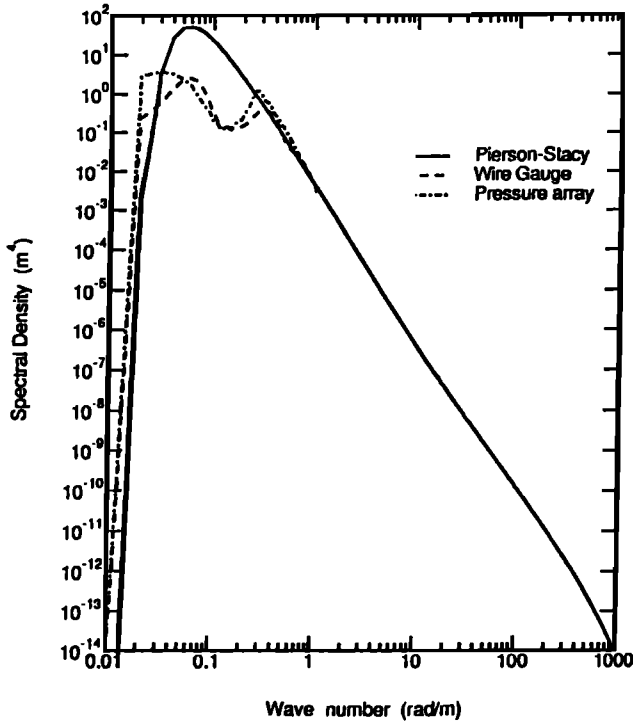


Fig. 6. Comparison of the Pierson-Stacy wave number spectrum for a wind speed of 10.2 m/s with wave number spectra constructed from measured frequency spectra.

$$\mathcal{F}_W(\phi_k) = \cos^4 [(\phi_k - \phi_W)/2] \quad (17)$$

with ϕ_W being the wind direction, for the entire Pierson-Stacy spectrum. For the measured spectra, an examination of the pressure sensor data showed that the peak in the measured spectra at about 0.1 Hz is due to swell waves propagating toward shore (270°), and that the 0.27-Hz peak corresponds to wind waves aligned roughly with the wind (toward 84° T). We have therefore used $\mathcal{F}_W(\phi_k)$ to describe the angular dependence of the “measured” wave number spectra for wave numbers corresponding to frequencies greater than 0.18 Hz. For the low-frequency swell component of our “measured” spectra, we have chosen a somewhat narrower angular dependence of the form

$$\mathcal{F}_S(\phi_k) = \cos^6 [(\phi_k - \phi_S)/2] \quad (18)$$

where ϕ_S is the swell direction. This particular functional form has no special significance except that it is narrower than the wind-wave angular term and was relatively easy to implement in our scattering code. In fact, it should be mentioned here that the appropriate angular dependence of the 2D wave number spectrum is one of the major uncertainties in the development and testing of scattering models. We hope that further analysis of SAXON data can provide some guidance as to the form of this dependence as a function of wave number and wind conditions [Shemdin, 1989; Herbers and Guza, 1990]. Figure 6 shows the behavior of the magnitude of the three wave number spectra, $\chi(|\mathbf{k}|)$, constructed as discussed above over the full wave number range used in our computations.

We have used the three wave number spectra discussed above as input to our scattering model to compute the corresponding V - V and H - H polarization mean cross sections and

Doppler spectra. The computed polarization ratios, σ_{HH}/σ_{VV} , corresponding to the Pierson-Stacy spectrum, the augmented wire gauge spectrum, and the augmented pressure sensor array spectrum are 0.82, 0.79, 0.81, respectively. These values are not out of line with our expectations for backscattering at 20° incidence and 10 m/s winds. Due to the (± 2 dB) uncertainty in the relative calibration of the V - V and H - H channels discussed above, detailed comparison of these values with the measured ratio is not too meaningful.

We can, however, compare the measured and calculated Doppler spectra for both polarizations. In Figure 7 we show comparisons of the predicted Doppler spectra using the Pierson-Stacy spectrum, the augmented wire gauge spectrum, and the augmented pressure sensor array spectrum in Figures 7a and 7b, 7c and 7d, and 7e and 7f, respectively. To facilitate comparison, we have normalized the calculated spectra to match the measured spectral peak for each case. (The error bars on the measured spectra are the same as those shown in Figure 4.) It can be seen from this figure that the Doppler spectra computed using the Pierson-Stacy height spectrum show the poorest agreement with the measured spectra. In particular, the center frequency is too high and the width is too broad. The agreement is much more satisfactory for the Doppler spectra computed using either of the surface wave spectra that have been augmented using the in situ data. This is because the width and center frequency of the Doppler spectra are sensitive to the moments V^2 , α , and β in (13d)–(13f) which depend on the longwave spectral energy. As we have seen from Figure 5, the Pierson-Stacy spectrum overestimates this longwave energy as compared to the measured spectra. In Table 2 we list the center frequencies and widths obtained using each of the three wave number spectra. One can see from this table that the Doppler widths and center frequencies computed using either of the surface-wave spectra that are augmented by the in situ spectral data are in good agreement with the those found in the measured Doppler spectra. The computation using the pressure sensor spectra yield the closest agreement. The computation using a Pierson-Stacy surface wave spectrum, which assumes a fully developed wind waves and no swell, overpredicts both the width and center frequency of the Doppler spectrum. These results indicate the sensitivity of the Doppler calculations to the energy in the longwave portion of the surface wave spectrum. Thus it is necessary to have a good estimate of this spectrum in order to make accurate predictions of the backscattered field. We should mention here that our computations are in fact not very sensitive to the low-frequency swell component seen at about 0.1 Hz in both the measured spectra shown in Figure 5, regardless of our choice for the angular dependence, $\mathcal{F}_S(\phi_k)$, in (18). This is because the longwave moments that determine the form of the Doppler spectrum are weighted toward higher wave numbers. (See (13d)–(13f).) For the augmented spectra discussed here, these moments are dominated by the wind-wave peak at 0.27 Hz. Swell will contribute significantly to the Doppler characteristics only when the power in the swell region of the spectrum provides the dominant contribution to these moments. Thus the 0.1-Hz swell peak in the measured spectra is not strong enough to produce the low-frequency tail observed in the measured spectra. Aside from this minor deficiency, the agreement between the calculated and the measured Doppler spectra is quite satisfactory (when the proper surface wave spectra is

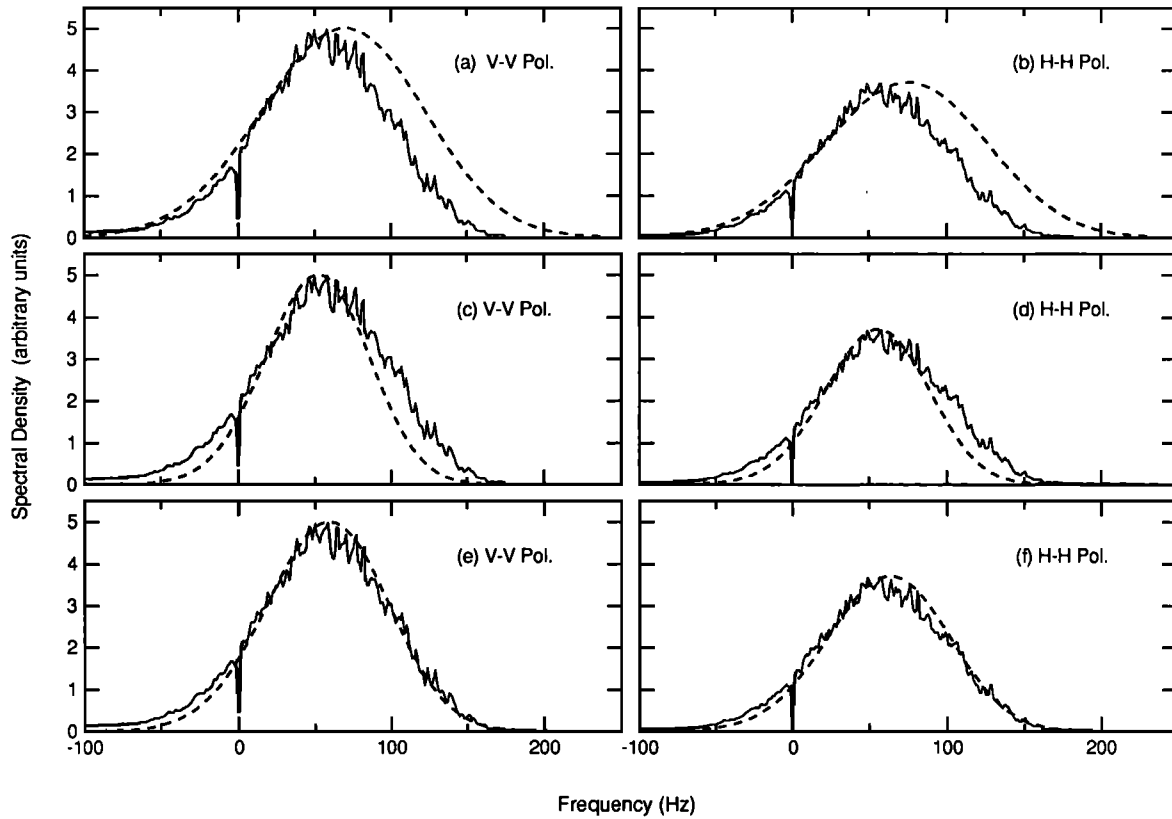


Fig. 7. Comparison of measured Doppler spectra with predictions using (a, b) an empirical wave number spectrum, (c, d) the augmented wire gauge spectrum, and (e, f) the augmented pressure sensor array spectrum.

used). This gives us confidence that our scattering model contains most of the essential physics required to describe K_u -band backscatter at 20° .

5. SUMMARY AND CONCLUSIONS

In this paper we have presented an analysis of the properties of coherent K_u -band radar backscattered from about a 2.5-m^2 patch on the ocean surface at the relatively small incidence angle of 20° . Our data, collected during the ONR-sponsored SAXON experiment at the Chesapeake Bay Light Tower, were augmented by concurrent in situ measurements of the longwave portion of the surface wave spectrum as well as measurements of the mean surface current and local wind velocity. These in situ data provided some of the surface truth necessary to initialize our scattering model so that we could compare its predictions with the measured radar data.

The radar data product which forms the basis of our analysis is an ≈ 20 -min time series of 1-s Doppler spectra.

The center frequency of these spectra migrate from less than -50 Hz to more than 100 Hz. This migration is due to the changing orbital velocity over the phase of the long (compared to the radar footprint) surface waves. (The 28-Hz offset of this frequency spread is due to the mean surface current plus the motion of the K_u -band Bragg waves.) Since the long wind waves were moving toward the radar, the front face of the waves had a positive line-of-sight velocity, and produced a positive-frequency Doppler offset. The front face of these waves is tilted toward the radar so that the backscattered power is also greater. Thus the Doppler spectra with positive Doppler offsets are expected to contain more power than those with a negative offset. This feature was clearly observed in our data. Also, we have separated the 1-s Doppler spectra into eight equally populated frequency bins spread across the entire observed range. The average widths of the spectra in each of these bins were found to be nearly equal.

These 1-s spectra have been averaged over the entire time series to produce mean Doppler spectra. Because the 1-s spectra with positive frequency have more power, this mean is weighted toward positive frequencies, and the center frequency of our mean Doppler spectra are about 58 Hz. The width of the mean spectra are about 98 Hz. This value is a measure of the extent of the frequency migration of the 1-s spectra again weighted toward the positive frequencies that contain the most power.

We have also presented in this paper a time-dependent scattering model which we have used to compare predicted Doppler spectra with the measurements. This model is initialized using in situ measurements of the surface spec-

TABLE 2. Doppler Spectrum Parameters

Spectrum	Full Width at Half Maximum, Hz		Center Frequency, Hz	
	V-V	H-H	V-V	H-H
Measured	99	98	58	59
Pierson-Stacy	125	123	70	75
Wire gauge	79	78	51	54
Pressure array	93	92	59	63

trum, and the time dependence is based on the assumption of free-wave dispersion of the spectral components. The effect of the longwave surface slope on the backscattered field is automatically included in the model with no explicit assumptions about a tilt-modulation transfer function. When the empirical Pierson-Stacy surface wave spectrum corresponding to the measured wind was used to initialize our scattering model, the resulting predictions yielded overestimates of the center frequency and width of the mean Doppler spectra as compared with the data. This is because the empirical surface wave spectrum, which is based on the assumption of a fully developed sea, provided too much power to the long waves present during our data collection. This assessment is based on a comparison of the empirical spectrum with in situ measurements of the longwave frequency spectrum collected concurrently with the radar data. When we used these in situ measurements of the longwave surface spectrum augmented by the empirical spectrum in the shortwave region (where no direct measurements were available during the time of our data collection) to initialize our scattering model, we have found that the model predictions and the measured Doppler spectra agreed quite well. In particular, the model properly accounted for the large Doppler shift due to the heaving motion of the longwave surface and also predicted the proper Doppler width.

The success of this study gives us confidence that our model can describe many of the essential features of coherent radar return at low to moderate incidence angles. The model, of course, needs to be tested for different environments and geometries. In fact, we have also collected some cross-wind data that we plan to analyze in a similar manner in the near future. This analysis could give us some indication of the model's sensitivity to the angular dependence of the surface wave spectrum. Furthermore, we expect that at higher incidence angles where the tilting of the longwave surface becomes less important, the sensitivity of the backscattered field to the modulation of the shortwave portion of the spectrum by the longwave orbital velocity (the hydrodynamic modulation) will become important. The inclusion of this hydrodynamic modulation is straightforward when the modulation transfer approach is valid (see, for example, *Alpers et al.* [1981] or *Plant* [1989]) and will be the next refinement to our scattering model.

Finally, we should mention that we have recently found a way to use our scattering model along with the longwave spectral measurements to simulate the K_u -band backscatter time series. A preliminary comparison of the backscatter statistics obtained from our simulation with that obtained from the measured data is quite encouraging. Both the simulation and the data suggest that the distribution of the backscattered field has a much longer tail than that from an exponential distribution which would result if the backscattered field were Gaussian distributed. The backscatter statistics depend in a complicated way on such parameters as radar frequency, incidence angle, and footprint size as well as the environmental conditions. We are planning to investigate the sensitivity of the backscattered field to these parameters during the forthcoming continuation of the SAXON Experiment on the Forschungsplattform Nordsee. The resulting data should provide even more stringent constraints on our scattering model.

Acknowledgments. This paper would not have been possible without the cooperation of the many of the SAXON investigators who provided us with their data, usually before publication. In particular, we want to acknowledge Andy Jessup and Ken Melville at MIT for providing the wire gauge data as well as the meteorological data; Tom Herbers and Bob Guza at Scripps Institute of Oceanography for providing the pressure sensor data; and M. P. Abreu, T. P. Stanton, and E. B. Thornton of the Naval Postgraduate School in Monterey, California, who collected the background current data which was kindly provided to us by Ivan Popstefanija of the University of Massachusetts. All of the persons listed above as well as the SAXON principal investigator Omar Shemdin of Ocean Research and Engineering in Pasadena, California, were always willing to answer our questions about the data and all aspects of the experiment. Finally, special thanks go to Frank Herr and Hans Dolezalek who managed the SAXON Program for the Office of Naval Research. They have provided us much advice and constant encouragement throughout the course of this investigation.

REFERENCES

- Abreu, M. P., T. P. Stanton, and E. B. Thornton, Finescale current profiles and directional wave spectra during SAXON 1988, paper presented at 1990 Ocean Sciences Meeting, AGU, New Orleans, La., February 12–16, 1990.
- Alpers, W., D. B. Ross, and C. L. Rufenach, On the detectability of ocean surface waves by real and synthetic aperture radar, *J. Geophys. Res.*, **86**, 6481–6498, 1981.
- Bjerkaas, A. W., and F. W. Riedel, Proposed model for the elevation spectrum of a wind-roughened sea surface, *Rep. TG-1328*, Johns Hopkins Univ. Appl. Phys. Lab., Laurel, Md., 1979. (Available as NTIS ADA083426 from Natl. Tech. Inf. Serv., Springfield, Va.)
- Herbers, T. H. C., and R. T. Guza, Estimation of directional wave-spectra from multicomponent observations, *J. Phys. Oceanogr.*, **20**(11), 1703–1724, 1990.
- Holliday, D., Resolution of a controversy surrounding the Kirchhoff approach and the small perturbation method in rough surface scattering theory, *IEEE Trans. Antennas Propag.*, **35**, 120–122, 1987.
- Melville, W. K., J. A. Kong, R. H. Stewart, W. C. Keller, A. T. Jessup, D. Arnold, and A. Slinn, The measurement and modelling of sea-state bias in SAXON, in *Proceedings of the 1989 International Geoscience and Remote Sensing Symposium (IGARSS'89)*, vol. 3, pp. 1922–1925, IEEE, New York, 1989.
- Pierson, W. J., and R. A. Stacy, The elevation, slope, and curvature spectra of a wind roughened sea surface, *NASA Rep. CR-2247 N74-15068*, 1973.
- Plant, W. J., The modulation transfer function: Concept and applications, in *Radar Scattering From Modulated Wind Waves*, edited by G. J. Komen and W. A. Oost, pp. 155–172, Kluwer Academic, Boston, Mass., 1989.
- Plant, W. J., and W. C. Keller, Evidence of Bragg scattering in microwave Doppler spectra of sea return, *J. Geophys. Res.*, **95**, 16,299–16,310, 1990.
- Shemdin, O. H., Sar X-band and ocean nonlinearities: Overview, in *Proceedings of the 1989 International Geoscience and Remote Sensing Symposium (IGARSS'89)*, vol. 3, p. 1503, IEEE, New York, 1989.
- Thompson, D. R., Calculation of radar backscatter modulations from internal waves, *J. Geophys. Res.*, **93**, 12,371–12,380, 1988.
- Thompson, D. R., Doppler spectra from the ocean surface with a time-dependent composite model, in *Radar Scattering From Modulated Wind Waves*, edited by G. J. Komen and W. A. Oost, pp. 27–40, Kluwer Academic, Boston, Mass., 1989.
- Valenzuela, G. R., Theories for the interaction of electromagnetic and oceanic waves—A review, *Boundary Layer Meteorol.*, **13**, 61–85, 1978.

B. L. Gotwols and D. R. Thompson, Applied Physics Laboratory, Johns Hopkins University, Johns Hopkins Road, Laurel, MD 20723. W. C. Keller, U.S. Naval Research Laboratory, Washington, DC 20375.

(Received July 3, 1990;
revised October 9, 1990;
accepted October 9, 1990.)